PHYSICAL REVIEW C VOLUME 55, NUMBER 1 JANUARY 1997

Excitation energies and temperatures of hot nuclei produced in the reactions of ^{63}Cu+^{197}Au at 35*A* MeV

R. Wada, R. Tezkratt,* K. Hagel, F. Haddad,† A. Kolomiets, Y. Lou,‡ J. Li, M. Shimooka,§ S. Shlomo, D. Utley, B. Xiao, N. Mdeiwayeh, and J. B. Natowitz
Cyclotron Institute, Texas A&M University, College Station, Texas 77843

Z. Majka, J. Cibor, T. Kozik, and Z. Sosin
Institute of Physics, Jagellonian University, ul. Reymonta 4, 30-059 Kraków, Poland

(Received 31 July 1996)

Observations of heavy remnants emitted at forward angles with high velocities and high associated particle multiplicities have been used to select central collisions of 35*A* MeV ^{63}Cu with ^{197}Au. The data indicate that these remnants, both fission fragments and evaporation residuelike products, result from the deexcitation of nuclei with $A\sim225-240$ having excitation energies of $\sim$ 800–1300 MeV. Similar particle multiplicities are observed for both evaporative and fission decay channels. Modeling the results with hybrid codes which treat entrance channel dynamics followed by sequential statistical decay requires the inclusion of some delay in the fission channel to produce heavy remnants with mass $A\geqslant130$, but the trend of the predicted velocities of these heavy remnants is different from that of the experiments. Calculations with a dynamic model based on the molecular dynamics approach have also been performed and lead to similar results. He and Li isotope yield ratios and the apparent temperatures derived from those ratios are similar to those previously reported for excited nuclei in this mass region. Temperatures derived from other yield ratios are also similar once a self-consistent treatment, taking into account population and decay of known excited states, is applied. The derived temperatures show little variation with excitation energy, suggesting that a limiting temperature may be reached at relatively low excitation energy, although the interpretation of this result and the determination of the actual initial value of this temperature is model dependent. Comments on the application of the double isotope yield ratio technique to extraction of the nuclear caloric curve are made. [S0556-2813(97)01101-1]

PACS number(s): 24.60.Dr, 25.70.Gh

I. INTRODUCTION

The properties of atomic nuclei with large excitation energies have been under extensive investigation in recent years [1–5]. In the low energy range ($E/A\leqslant10$ MeV), fusion processes dominate, with most of the incoming kinetic energy dissipated into excitation energy of the fused system [6,7]. As the projectile energy increases, more and more excitation energy is deposited inside the nucleus but the fusion process progressively vanishes and is replaced by other processes [8–10]. Recently, in the work of Utley *et al.* on ^{40}Ar+^{232}Th at 40*A* MeV, we reported the observation of heavy reaction products, both fission fragments and residues at small forward angles [11]. The derived excitation energies associated with these heavy remnants reached approximately 900 MeV. While such heavy products have been observed also in other works [12–15], ambiguities still remain regarding the relative contributions of evaporation processes and binary deep inelastic processes to the production of these heavy products.

We present here the results of an experiment in which the production and deexcitation of heavy remnants from the reaction ^{63}Cu+^{197}Au at 35*A* MeV have been studied. The principal decay modes associated with both fission fragment and heavy residue production are established and primary excitation energies are determined. The results are compared with those of model calculations based on both dynamical and statistical approaches [10,16,17]. Apparent temperatures derived from double isotope ratios are compared with those previously reported for similar systems [18–21]. The interpretation of these ratios is discussed.

The paper is organized as follows: In Sec. II we present the experimental procedure. Section III is devoted to the experimental results. In Sec. IV results of model calculations are presented. In Sec. V we present a reconstruction of the energy deposition and mass from the experimental results. We then present and discuss temperature determinations from double isotope ratio measurements. A summary of our results and conclusions are given in Sec. VI.

II. EXPERIMENTAL PROCEDURES

Two experiments were performed at the Texas A&M K500 Superconducting Cyclotron facility. In both experiments a ^{63}Cu beam of 2205 MeV energy was incident on a self-supporting ^{197}Au target having an areal density of 450 μg/cm^2. Neutrons were measured by a 4π neutron ball detector and charged particles by a large number of individual detectors. The detectors are described in more detail below.

---

*Also at 28 Chemin de la Bourdette, 31400 Toulouse, France.

†Also at Subatech, 2 Rue de la Houssinière, 44072 Nantes Cedex, France.

‡Also at Human Genome Project, Lawrence Berkeley National Laboratory, 1 Cyclotron Road, Berkeley, CA 94 720.

§Also at Faculty of Science, Kyoto University, Kyoto, Japan 606.

A. Neutron ball detector

The neutron multiplicity measurements were carried out using a 4π Gd-loaded liquid scintillator detector, the Texas A&M Neutron Ball (NBL) [22]. This device, with a spherical shape and a volume of 1800 liters, consists of two hemispheres (top and bottom) and eight radial wedges arranged in the horizontal plane (each covering 40° in the lab). The forward wedge covering ±20° relative to the beam is normally absent and replaced with an extension of the reaction chamber which allows time of flight measurements to be carried out. Light produced by the scintillation process following neutron capture is detected during a 100 μs counting gate by 18 phototubes. During the experiment background measurements are made by opening a second 100 μs gate following the counting gate. In order to reduce the background a twofold coincidence is required for the photomultiplier signals in the top and bottom hemisphere. The background correction was made by subtracting the average background during each run from the average total multiplicity observed in the counting gate. For some runs the correction also was made on an event by event basis for a comparison and both results agreed within error bars. The typical average background count was 1.4–3.7, depending on the beam intensity. Most coincidence results presented in this paper were taken with a background of 3.7. The detection efficiency of such a device depends on the kinetic energies and angular distributions of the neutrons, the amount of the liquid scintillator and the Gadolinium concentration, which is 0.3% by weight in our detector. A Monte Carlo simulation, performed with a modified version of the codes DENIS [23] and EUGENE [10], is used to estimate the detection efficiency for neutrons emitted from sources of different velocities and temperatures. The neutron detector is more efficient for the neutrons emitted from the slow targetlike source than for those emitted from the projectilelike fragments. More details on these calculations can be found in [11]. Efficiency calibrations of the neutron ball were carried out with a radioactive source, ^{252}Cf. The efficiency for these neutrons was found to be 85%. The measured values were then used to normalize the efficiency curve deduced from the simulations of the neutron ball efficiency, using the code DENIS. The background corrections of our measurements are made by subtracting the average background values from the average multiplicities. On the observed multiplicity values we apply another 3% correction to neutrons which are not captured in the true counting gate and bleed over into the background gate.

B. Charged particle detectors

The scattering chamber of the neutron ball has an extension in the forward direction with a ±20° opening along the beam axis. In the first experiment we placed a 900 mm^2, 200 μm thick silicon detector (RES) at +6° relative to the beam axis in the horizontal plane and 170 cm away from the target position. This detector was used for energy and time of flight measurements of the heavy fragments emitted at forward angles. For the time of flight measurements the neutron ball fast signal, which has a typical time resolution of ~3 ns, was used as a timing signal. Overall time resolution of the time of flight measurement for heavy fragments was ~3.5 ns, which give a mass resolution of ~6% for the fragments with a velocity of 1.5 cm/ns. The energy and time of flight calibrations were performed using radioactive sources ^{241}Am and ^{252}Cf and by scattering 2A MeV ^{136}Xe and ^{181}Ta beams with a thick ^{197}Au target. In order to achieve accurate mass and velocity determinations for heavy fragments, plasma delay, and pulse height defect corrections have been made. In order to detect projectilelike fragments, a hodoscope (HOD), made of a thin silicon detector (300 μm) backed by a 5 mm CsI(TI) scintillator crystal with covering angles from $-5°$ to $-7°$, was used.

A spherical ball (BALL) of 10 cm radius surrounded the target and held a set of 35 $\Delta E-E$ telescopes, covering the polar angles between 60° and 156° [24]. These detectors were used for the detection of light charged particles and intermediate mass fragments (IMF's). The ΔE detectors were gas ionization chambers operated with a flow of isobutane, C_4H_{10}, maintained at a constant pressure of 135 torr. The E detectors were 2 mm thick, 31 mm diameter, Li-drifted silicon detectors.

In a second experiment, two large ionization chambers with entrance windows of 15 cm×11 cm were used to detect heavy fragments at forward angles between 6° and 15°. The ionization chambers consisted of ΔE (2 cm) and E (18 cm) sections. The ΔE part was divided into seven sections for angular distribution measurements. The chambers were set symmetrically on the two sides of the beam axis at a distance of 100 cm from the target. The timing signals were obtained from the ΔE detectors. In coincidence with heavy fragments, five gas-Si-CsI telescopes (TEL's) [25] were set at 44°, 72°, 110°, 128°, and 148°, each having a covering angle of ±10°. Each telescope consisted of a gas IC, 300 μm Si, 1000 μm Si, and 2 cm CsI. The Si detectors (5 cm×5 cm) are divided into four sections and the solid angle of each section is 24 msr. In the telescopes used in both experiments, hydrogen and helium isotopes are clearly identified. The atomic numbers of the fragments with $Z\geqslant 3$ are also clearly established. Mass identification of He and Li isotopes in the second experiment allowed the determination of ''temperatures'' using the double isotope ratio technique [26].

Several different triggers were used in the data acquisition. The prescaled NBL, itself, was used as a single trigger and coincidences between NBL and other triggers such as RES, HOD, BALL, and TEL were also used as event triggers.

III. EXPERIMENTAL RESULTS

A. Neutron multiplicities

The neutron multiplicity distribution reveals much about the dissipation profile of the reactions. Figure 1 shows the observed neutron multiplicity distribution after background correction (dots). No detection efficiency corrections have been made. This distribution exhibits a characteristic shape with two primary components [27]. The first component, centered at lower multiplicities, corresponds to neutron emission from low excitation energy peripheral collisions as well as a large background contribution. The second, peaking near $\langle M_n \rangle = 25$ corresponds to highly damped collisions in which much larger excitation energy is deposited. One should note, however, that on the lower multiplicity side, the spectrum is significantly affected by background because the

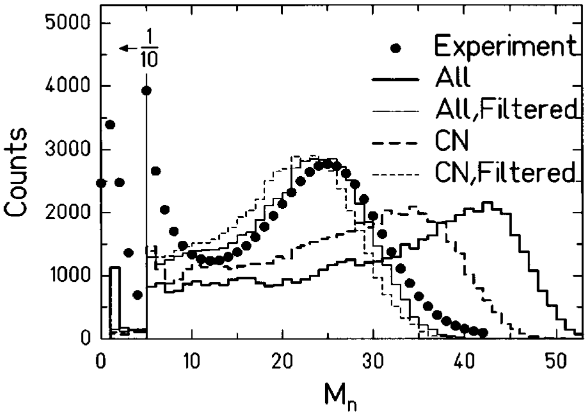

FIG. 1. The detected neutron multiplicity distribution, corrected for background but not for detection efficiency, is indicated by dots. Data below $M_N=5$ are devided by a factor of 10. Also shown for comparison are the calculated distribution of total neutron multiplicity obtained with the code EUGENE-GEMINI (thick solid line) and the calculated multiplicity distribution for neutrons evaporated from the CN-like source (thick dashed line). The distribution represented by the thin solid line is the net distribution expected when the neutron ball detection efficiency is applied to the calculated total distribution. The thin dashed line indicates the histogram of detected neutrons which results from a similar filtering of the neutron distribution from the CN-like source.

spectrum is taken in the self-triggered mode. The histograms present results of calculations discussed in Sec. IV.

The peripheral collisions are characterized by the emission of projectilelike fragments at forward angles with velocities slightly lower than the beam velocity [9,28]. In our experiment projectilelike fragments were detected, and their charge identified, by the hodoscope detector. In Fig. 2 background corrected average neutron multiplicities are presented as a function of charge for both the projectilelike fragments and for fragments detected at larger angles [28]. Experimental results are shown by symbols (same data are used in both figures). At $\theta=4°$, the increase of the neutron multiplicity with decreasing charge of the projectile remnant is characteristic of massive-transfer reactions and reflects the fact that the more violent the collision the more excited is the remaining intermediate nucleus. The fragments of small atomic number detected at $\theta=4°$ show a comparable neutron multiplicity to those associated with fragments detected at larger angles, which suggests that these fragments have a similar origin. The lines represent results of the calculations discussed in Sec. IV.

B. Heavy products

Focusing on reaction products at small forward angles further enhances our ability to select the most dissipative reaction mechanisms [11]. Figure 3 presents the mass distribution of products detected at $\theta=6°$. Solid points (same experimental data are used in both figures) represent the experimental points. Histograms are the results of model simulations discussed below. The experimental result shows a significant yield of products with a mass $A \geqslant 120$. To further explore the nature of the heavy products a contour plot of mass versus velocity for the heavy fragments detected at $\theta=$ 6° is shown in Fig. 4(a). The products with large yields in the left-upper corner are the projectilelike fragments. Two other prominent groups of fragments with mass greater than the projectile mass ($A=63$) are observed. The group centered at $A\sim70$–100 and velocity $v\sim1.5$ cm/ns, corresponds

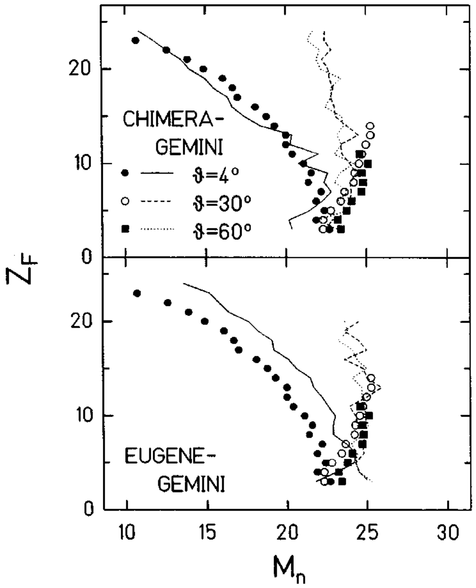

FIG. 2. Average detected neutron multiplicities as a function of the atomic number for fragments observed at $\theta=4°$, 30°, and 60°. Symbols show experimental results and lines are from the CHIMERA-GEMINI simulation (top) and the EUGENE-GEMINI simulation (bottom).

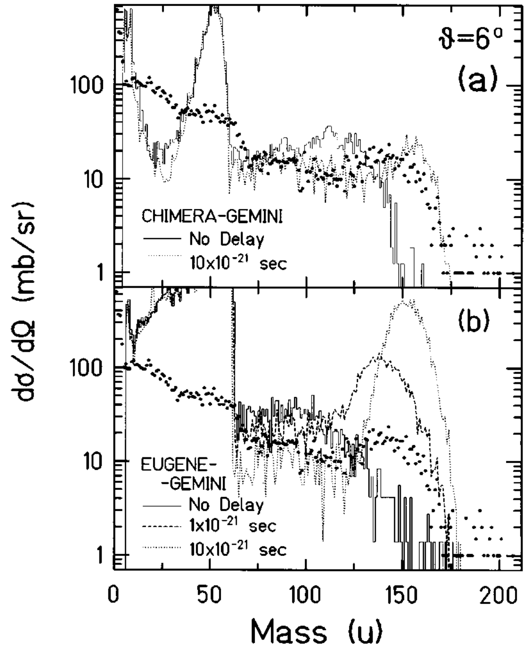

FIG. 3. The product mass distribution at $\theta=6°$. Dots represent the same experimental data in both figures. (a) The results from the CHIMERA-GEMINI simulation. The solid and dashed histograms are the results without fission delay and with a fission delay of 10×10^{-21} s, respectively. (b) The results from the EUGENE-GEMINI simulation. The solid, dashed, and dotted histograms are the results without fission delay, with a fission delay of 1×10^{-21} s and with a fission delay of 10×10^{-21} s.

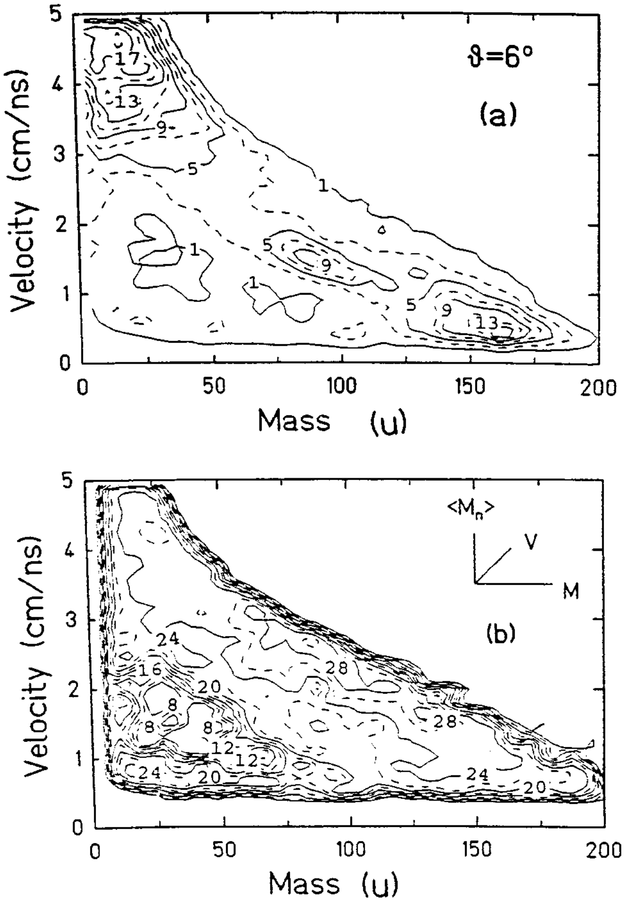

FIG. 4. Correlations between velocity, mass and neutron multiplicity for products detected at $\theta = 6°$. (a) Velocity vs mass diagram for products with $M_n \geqslant 15$. The contours are shown for changes of every 2 mb/sr/(cm/ns). (b) Average associated neutron multiplicities for fragments of a given mass and velocity. Each contour shows an average number of neutrons detected for a given velocity and mass of the fragment. The contouring is linear.

to fissionlike fragments. The yield of these fragments extends up to $v \sim$ 3 cm/ns. A group of heavier fragments with $A \sim 120$–170 and $v \sim 0.5$ to nearly 2.0 cm/ns is also seen.

The average detected neutron multiplicity $\langle M_n \rangle$, corresponding to the observed fragments in the velocity-mass plane in Fig. 4(a), is shown in Fig. 4(b). The associated neutron multiplicities for the heavy fragments at the lower right of the upper figure are $\langle M_n \rangle \sim 20$ at a velocity $v \sim 0.5$ cm/ns and gradually increase as the velocity increases. At higher observed velocities ($v \sim 1.75$ cm/ns), $\langle M_n \rangle$ reaches 28. A similar trend of multiplicity increasing with velocity is observed for the fissionlike fragments, but with a shift in the velocity scale, i.e., $\langle M_n \rangle$ is around 20–22 for the fissionlike fragments at $v \sim 1.5$ cm/ns and increases as the velocity increases. For the fission fragments the average neutron multiplicity reaches a maximum of $\langle M_n \rangle \sim 28$–30 at velocities near 3 cm/ns. The velocity shift is easily understood as indicating that the heavy products and fission fragments detected at the most forward angles results from events with similar momentum transfers and excitation energies. For the fission fragments, in this case, the additional velocity from the Coulomb energy reflects on their kinetic energies in the frame of the emitter, which is an order of 1–1.5 cm/ns.

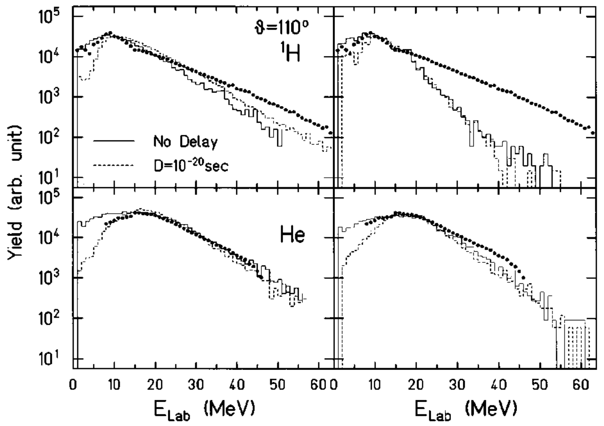

FIG. 5. Proton (top) and helium (bottom) energy spectra at $\theta = 110°$. The helium spectrum includes ^{3}He and ^{4}He. The solid and dashed histograms are results without delay and with a fission delay of 10×10^{-21} s, respectively, for the EUGENE-GEMINI simulation (left) and the CHIMERA-GEMINI simulation (right). The calculated results are normalized to the experimental data individually.

C. Charged particles

The deexcitation of the excited nuclei has been further investigated using measurements of the associated charged particle and fragment emission. This is important since the neutron emission process becomes less probable at high excitation energies, reflecting the increasing competition from charged particle emission [11,14,29].

Typical light charged particle spectra at $\theta = 110°$ are shown in Fig. 5 (dots) with the results of model simulations (histograms). (The same data are used in the left and the right figures.) In the figure the helium spectrum includes ^{3}He and ^{4}He, because no separation was achieved in the low energy region. The ^{3}He contribution to the spectrum is about 5%. In Fig. 6 carbon energy spectra at different angles are shown as typical IMF spectra.

Light particle and IMF multiplicities associated with the heavy products were measured as a function of the heavy product velocity. The results are given by the solid symbols in Fig. 7. On the left side of Fig. 7 the multiplicities observed in coincidence with fragments with mass $60 \leqslant A \leqslant 90$ are plotted. On the right side the multiplicities observed in coincidence with the heavy products, $130 \leqslant A \leqslant 170$, are given. In order to minimize a contribution from the preequilibrium emission, the proton and α multiplicities have been evaluated from the telescopes set at $\theta = 110°$–148° in the second experiment, assuming isotropic emission from a single source. As seen in the top of Fig. 5 the proton spectrum shows a hard component even at 110°, which may originate from the preequilibrium emissions. The possible contribution of the preequilibrium emission to the evaluated proton multiplicity is estimated to be at most 30% at $\theta = 110°$ and smaller for the larger angles by comparisons with the simulated results discussed below. No such contribution is observed in the α spectrum. The IMF multiplicity is evaluated from the telescopes at 72° and 110°, also with isotropy assumed. The yields of charged particles observed show a significant variation with velocity, reflecting a broad range of excitation energies leading to these reactions. The yields observed in both parts of the figure are similar. For the heavy

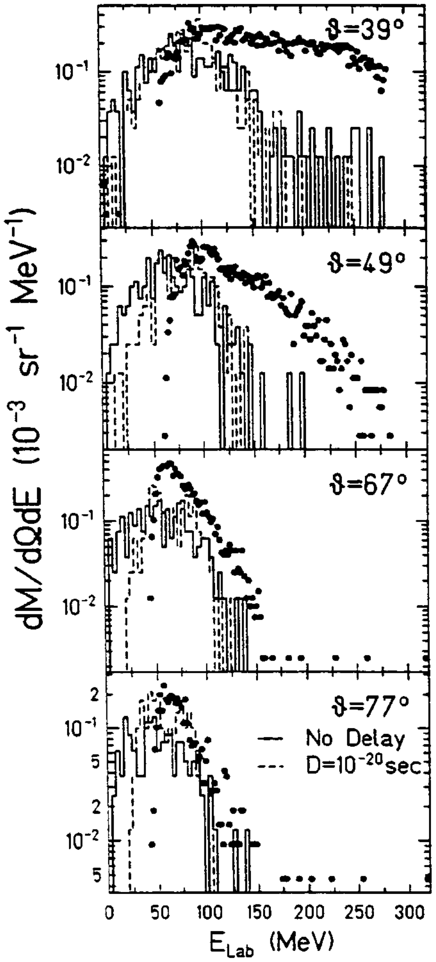

FIG. 6. Carbon energy spectra at different angles as indicated in each figure. The solid and dashed histograms are results of the CHIMERA-GEMINI simulation without delay and with a fission delay of 10×10^{-21} s. The calculated results are normalized to the experimental data at $\theta=39°$.

residues at higher velocities the average neutron multiplicities are slightly lower and the average α multiplicities higher than for fission. The IMF multiplicities are not large. There might be some more catastrophic multifragmentation in our system, but selection of events with heavy products focuses on the processes in which a large remnant remains.

IV. MODEL SIMULATIONS

The experimental results have been compared with model calculations based on several reaction scenarios. In order to simulate an incomplete fusion process a model based on a massive transfer scenario is used. For this purpose, the EUGENE code [10] was selected. This code has been shown to be very successful in modeling similar collisions [11,30]. In this program, for a given impact parameter, the maximum number of nucleons from the projectile trapped in the target is obtained in the pure geometrical limit corresponding to the straight trajectory of the incoming projectile. Preequilibrium emission is then treated by following nucleon-nucleon collisions in the overlap region of the projectile and the target. The rest of the projectile is treated essentially as a spectator but receives a little excitation energy. Using this code, the properties of the primary excited nuclei, were generated for the impact parameter range of $0\leqslant b\leqslant12$ fm.

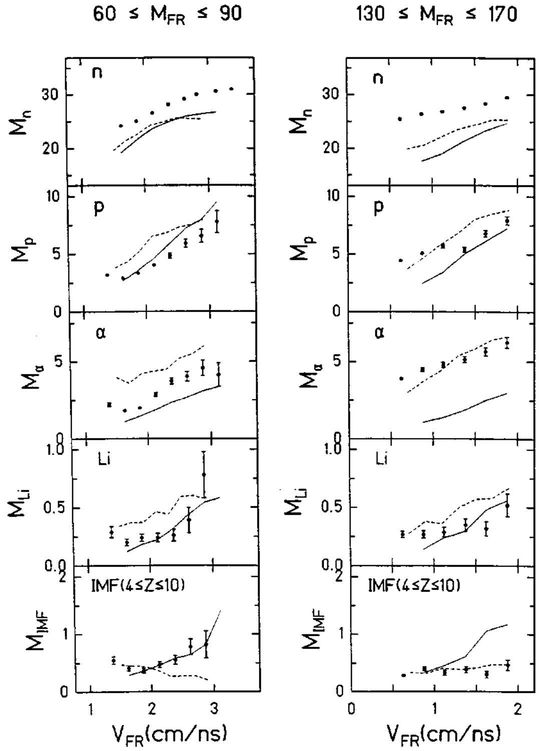

FIG. 7. Multiplicities of light particles and fragments as a function of the velocity of the heavy products in two different mass ranges. To determine light charged particle multiplicities only data from the backward angle telescopes have been employed. The IMF multiplicities are determined from detectors at 72° and 110°. Experimental results are indicated by the solid symbols. The solid lines show the results of the CHIMERA-GEMINI simulation and the dashed lines show the results of the EUGENE-GEMINI calculation.

The EUGENE code uses a simplified treatment of the entrance channel dynamics. In order to describe more complicated mechanisms in the entrance channel, we also used a code based on the molecular dynamics approach. The code CHIMERA [17], which was used, is a combination of the approaches taken by two recent models, the quantum molecular dynamics model (QMD) of Aichelin and Stöcker [31] and the quasiparticle dynamic model of Boal and Glasli [32]. CHIMERA has been applied successfully to study linear momentum transfer in heavy ion reactions in the intermediate incident energy range [33]. In that work the comparison of the model results with a substantial body of experimental data favored a soft equation of state. The calculations presented in this paper have been performed using the incompressibility of nuclear matter $K=200$ MeV. The need for a soft equation of state is also manifested in recent studies of linear momentum transfer for different effective potentials [34].

In the EUGENE simulation a hot composite nucleus formation is assumed by the massive transfer reaction process. Since our version of EUGENE does not treat angular momentum in the deexcitation cascade, the statistical decay of the primary composite nuclei was then followed using the code

GEMINI [16]. In the CHIMERA simulation a composite nucleus formation is observed for central collisions in a study of a log time period ($t \leqslant 3000$ fm/c). The program GEMINI, therefore, was also used as an afterburner for the CHIMERA code, because in the QMD approach, following the history of the excited primary reaction products to long times requires a very large amount of computing time. In the program GEMINI, thermal equilibrium is assumed and all particles are emitted sequentially. Light particle emission is treated by the Hauser-Feshbach formalism [35] and the emission of fragments with $Z \geqslant 3$ is treated by the transition state formalism [36]. Throughout this paper the level density parameter $a = A/10$ (A is the mass of the decaying system) is used, unless otherwise specified. Special care has been paid to establish the switching time to GEMINI in the CHIMERA calculation [37] by observing both the velocity of the fused system and the particle emission as a function of time. The combined system has the full center of mass velocity at a very early stage of the collision (0–20 fm/c). The velocity rapidly decreases up to 50 fm/c and becomes more or less constant after 100 fm/c. Observation of the calculated differential particle multiplicity indicates that the preequilibrium emission also ceases around 100 fm/c. For peripheral collisions another 100-200 fm/c is required for the system to break into two early stage binary fragments. In the following simulation, therefore, the change to the afterburner has been made at a time of 300 fm/c, unless otherwise specified. For the central collisions a switching time of 200 fm/c has been made for comparisons. No significant change in observables has been observed between the two choices of switching time.

In the following comparisons with the experimental results, all calculated events were filtered by the same conditions of the experimental setups, such as fragment detection angle, energy threshold, neutron ball detection efficiency and so on, unless otherwise specified.

A. Neutron multiplicities

With the kinematic information provided by the model calculations, a comparison of experimental and calculated neutron distributions is possible. The neutron multiplicity distribution calculated by the code EUGENE-GEMINI is shown together with the observed experimental distribution (dots) in Fig. 1. The histogram represented by a thick solid line and peaking near Mn ~ 43 shows the calculated neutron multiplicity from all sources, i.e., from projectilelike, preequilibrium, and compound nucleus-(CN) like sources. The histogram represented by the thick dashed line and peaking at Mn ~ 34 shows the calculated multiplicity distribution for the neutrons from the CN-like source alone. In order to compare the calculated multiplicities with the experimental results, the calculated primary neutron distributions have been filtered by the 4π neutron ball detection efficiency, incorporating both energy and geometry corrections and a normalization to the efficiency obtained for ^{252}Cf neutrons. The filtered results are shown by a thin solid histogram for the neutrons from all sources and by a thin dashed histogram for those from the CN-like source alone. Both results show a peak around Mn ~ 22–24. This indicates that our 4π neutron ball has much higher efficiency for the neutrons from the CN-like source. Only 1–2 neutrons from the preequilibrium source are detected, partially because there is no scintillator segment in the forward angle (±20°) and partially because these neutrons are more energetic.

The neutron multiplicity associated with IMF emissions has also been studied. The results of the CHIMERA-GEMINI calculation are shown in the top of Fig. 2 and those of the EUGENE-GEMINI calculation are shown in the bottom. The calculated results are presented by lines for IMF's detected at different angles. At $\theta = 4°$, the experimental trend is well reproduced in the CHIMERA-GEMINI simulation. The EUGENE-GEMINI simulation gives about two neutrons higher for a given charge of the projectilelike fragments. This suggests that the energy transfer and dissipation processes in the peripheral collisions are well taken care of in the CHIMERA code, but a little overestimated in the EUGENE-GEMINI simulation. On the other hand the trend of the neutron multiplicity with IMF emitted at larger angles is well reproduced by the EUGENE-GEMINI simulation for $Z_{\mathrm{IMF}} \geqslant 5$ and the CHIMERA-GEMINI simulation predicts slightly less neutrons for these IMFs.

The neutron multiplicities associated with heavy fragments are shown in the top row of Fig. 7. In that figure, associated neutron multiplicity is plotted as a function of fragment velocity, for a given experimental mass range. Dashed lines show results from the EUGENE-GEMINI calculation and solid lines show those from the CHIMERA-GEMINI code. Although the experimental trend is reasonably reproduced in both calculations, the filtered results of the code EUGENE differ from our observed experimental neutron multiplicity by about 3–5 neutrons. The difference becomes slightly larger for the CHIMERA calculation.

If one can assume the formation of an equlibrated composite nucleus, the associated neutron multiplicity gives a good measure of the excitation energy. To obtain a first estimate of the excitation energy deposited in the composite nucleus, the neutron multiplicity is plotted as a function of excitation energy in Fig. 8, using results of EUGENE-GEMINI. The composite nuclei with different excitation energies are generated by changing the impact parameter from 0 to 12 fm and the neutron multiplicity for a given excitation energy window is plotted as an approximate measure, neglecting differnces in the mass of the initial composite nucleus. (The initial mass for $E_x = 200$ is around 200 and that for $E_x = 1500$ is 240.) The total neutron multiplicities calculated as a function of the deposited excitation energies are presented both before and after the detection efficiency filter of the neutron ball. The multiplicities of the neutrons from all sources are plotted both without filtered (thick solid line) and with filtered (dashed line). The neutron multiplicities of the CN-like source are shown by thin lines. When the excitation energy increases the rate of increase of neutron multiplicity decreases, pointing to the important charged particle competition at high excitation energy. The detection efficiency of the neutrons from the CN-like source is 70–75 %. From the figure the observed highest neutron multiplicity of Mn = 28–30 would correspond to an excitation energy of 1500 MeV, but an uncertainty of a few neutrons causes a difference of a few hundred MeV in this energy range.

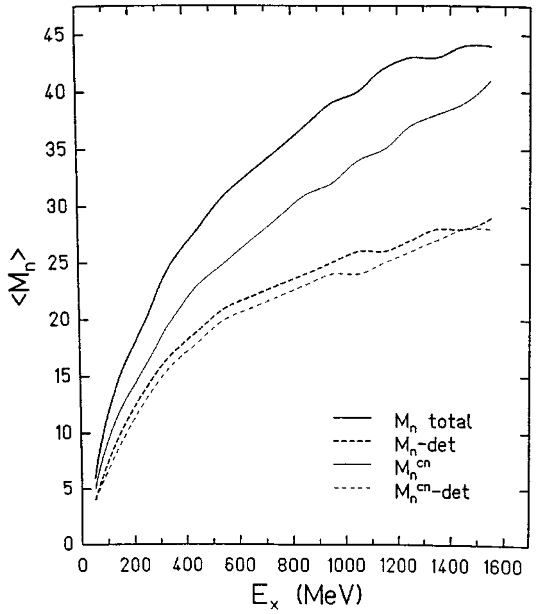

FIG. 8. Calculated average neutron multiplicity as a function of excitation energy obtained with the EUGENE-GEMINI simulation. A thick solid line indicates the average total neutron number $\langle M_n \rangle_{\text{total}}$ and a thin solid line is the average neutron number emitted from the CN-like source $\langle M_n \rangle_{\text{CN}}$. The corresponding results after efficiency filtering are indicated by a thick dashed line for $\langle M_n \rangle_{\text{total}}$ and by a thin dashed line for $\langle M_n \rangle_{\text{CN}}$.

B. Heavy remnant production

Recent studies of fission [38–40] have shown that dynamics plays an important role in that decay mode. At low excitation energy fission competes statistically with light particle emission, since the time required for light particle emission is comparable to the fission decay time. As the excitation energy increases, light particle emission becomes faster compared to the time required for fission to take place. Therefore it may be important to consider this effect in the present statistical decay calculations.

For a heavy nucleus with mass $A \geqslant 200$ and excitation energies more than a few hundred MeV, a standard statistical model predicts large decay widths for fission channels at the beginning of the deexcitation cascade and thus no heavy residues remain. In order to produce the fast forward directed heavy fragments with $A \geqslant 130$ in these calculations a fission delay can be incorporated. The fission process is delayed by suppressing decay channels with $Z \geqslant 3$ until the cumulative decay time of light particles reaches a certain time, called the fission delay time.

In the upper part of Fig. 9, calculated remnant mass versus associated neutron multiplicity, Mn (left), and polar angle in the laboratory frame, θ_{lab} (right), are shown in the case of the CHIMERA-GEMINI calculation without fission delay. No experimental filtering is applied in this figure. The remnants with mass $A \sim 150$ have a neutron multiplicity of around 30 but most of them are emitted around $\theta_{\text{lab}} \sim 50°$ and no remnants with mass around 150 are emitted at small angles. Thus these products in the calculation appear to originate in dissipative collisions while those observed at $\theta_{\text{lab}} = 6°$ appear to have a different origin. At larger angles there are, in fact, some heavy remnants produced. They originate from more peripheral collisions. The result for the remnants produced by incorporating a fission delay of 10×10^{-21} s is plotted in the lower part of Fig. 9. A large amount of heavy remnants with $A \geqslant 150$ and Mn $\sim$ 30–40 is produced as one can see on the left side of the figure and the these heavy remnants are emitted at more forward angles.

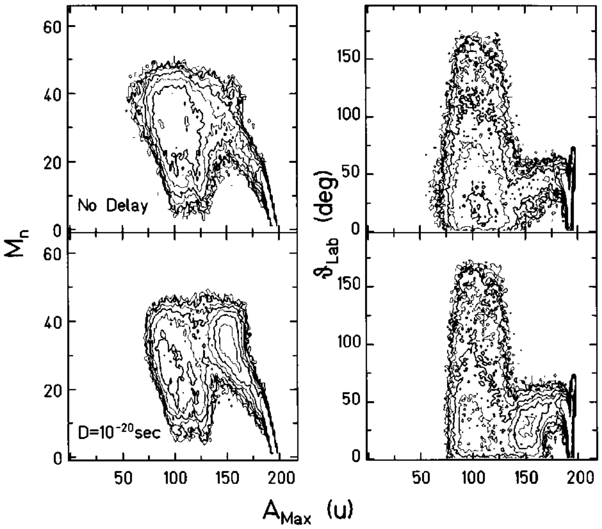

FIG. 9. Correlations between mass, neutron multiplicity and emission angle for the calculated heaviest products in the CHIMERA-GEMINI calculation. Neutron multiplicity given in the figure is total generated neutron multiplicity without any filtering. (Left) Mass vs neutron multiplicity diagram for no fission delay (top) and a fission delay of 10×10^{-21} s (bottom). (Right) Mass vs θ_{lab} for no fission delay (top) and a fission delay of 10×10^{-21} s (bottom).

The generated events are filtered by the experimental setup and plotted in the top of Fig. 3, where the calculated mass distributions at $\theta = 6°$ (histograms) are compared with the experimental results on an absolute scale. (The discrepancy below the projectile mass is caused by the fact that most projectilelike fragments punch through the Si detector in the experiments and their masses cannot be calculated properly.) The same velocity threshold as in the experiments ($v \geqslant 0.5$ cm/ns) is applied to the calculated results. The results with a fission delay of 10×10^{-21} s incorporated reproduce the experimental data very well for both fission fragments and heavy remnants, whereas in the results without fission delay the cross section of fission fragments is overestimated and no heavy remnants with $A \geqslant 150$ are produced. More detailed information appears in Fig. 10 where the calculated mass versus velocity is plotted. In the top of Fig. 10 the result without fission delay is plotted and in the bottom the result with fission delay is shown. In both parts of this figure fission fragments with masses around 100 and $v \sim 1.5$ cm/ns are rather well reproduced, as compared to the experimental results in Fig. 4(a). On the other hand, heavy remnants with velocity $v \sim 0.5$–1.0 cm/ns are missing in both figures. When the fission delay of 10×10^{-21} s is incorporated, heavy remnants are produced as seen in Fig. 3, but they have a peak at $v \sim 1.75$ cm/ns and show a quite different trend compared to that of the experimental results.

A similar study has been done for the EUGENE-GEMINI simulation. In the bottom of Fig. 3, the mass distributions

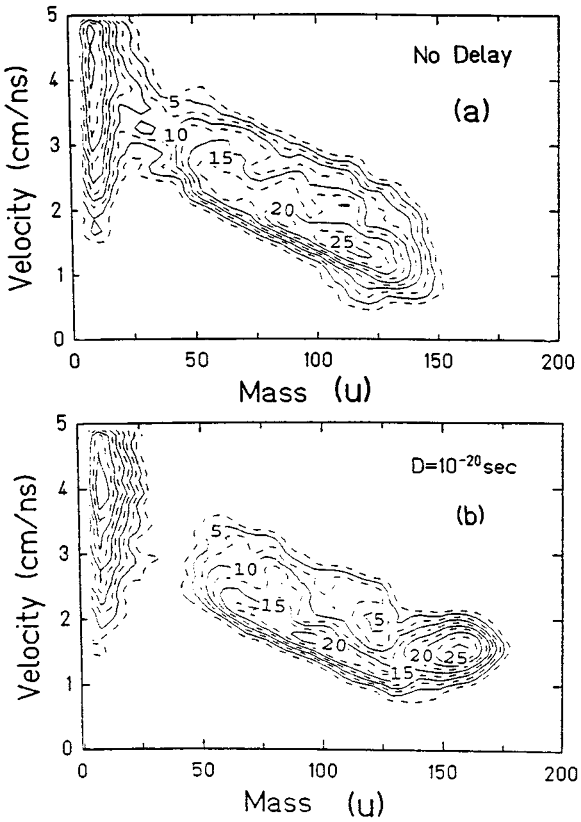

FIG. 10. Correlations between velocity, mass, and neutron multiplicity for products calculated from the CHIMERA-GEMINI simulation at $\theta = 6°$. The contours are shown for changes of every 2 mb/sr/(cm/ns). (a) No fission delay is employed. (b) A fission delay of 10×10^{-21} s is employed.

with different fission delays are shown by histograms. For the EUGENE-GEMINI simulation a large amount of heavy remnants is already produced for a fission delay of 1×10^{-21} s and the cross section of heavy remnants is higher by a factor of 5 than observed in the experiment (dashed histogram in the lower figure). For a delay of 10×10^{-21} s, the cross section is overestimated by a factor of 20–30. For the short delay of 1×10^{-21} in the CHIMERA-GEMINI simulation no notable difference from the results without fission delay is observed. This difference originates from the different average excitation energies given to the primary composite nucleus in the central collisions in the two models. In the EUGENE simulation the average excitation energy of the primary composite nucleus reaches a value of 1400 MeV, whereas in the CHIMERA simulation the average excitation given to the primary excited nucleus reaches only 800 MeV at 300 fm/c, when the switching to GEMINI is made. (A more detailed discussion of the excitation energy will be presented later in the following section.) The lifetime, τ, of the light particle evaporation in the GEMINI calculation is $\tau < 1.0 \times 10^{-21}$ sec for excitation energies above 600 MeV, for nuclei with $A \sim 200$–250. In the EUGENE-GEMINI simulation the primary composite nucleus cools down significantly during this short time period, to an excitation energy around 600 MeV, by light particle evaporation and the production of a relatively large number of nonfissioning heavy residues is more favored.

In conclusion both simulations failed to reproduce the heavy remnants observed at the forward angle in the experiment, even by incorporating fission delays. The role of the fission delay is not clear in this reaction system, because some important mechanisms, which lead to production of hot composite nuclei at forward angles, seem missing both in the EUGENE and CHIMERA simulations. This discussion is further addressed in Sec. VI.

C. Charged particle spectra and multiplicities

Calculated energy spectra of light charged particles observed at backward angles are compared with the experimental spectra in Fig. 5 for the EUGENE-GEMINI simulation on the left and the CHIMERA-GEMINI simulation on the right. The results with no fission delay are shown by solid histograms and those with a delay of 10×10^{-21} are shown by dashed histograms. The calculated spectra are arbitrarily normalized to the experimental spectra. For both simulations the low energy parts of the experimental spectra for protons and α particles are more or less reproduced similarly. On the other hand, on the higher energy side, a significant difference is observed, reflecting the different treatment of the entrance channel dynamics in both simulations. The EUGENE-GEMINI simulation reproduces the high energy part for both protons and α particles better than the CHIMERA-GEMINI simulation. This is interesting because in the CHIMERA calculation nucleon-nucleon collisions are treated microscopically and a better result is expected. As one can see in the figure, the low energy part of the spectrum is sensitive to the fission delay. This originates from the kinematical recoil effects in the decay process of an excited daughter fragment emitted from a parent nucleus. The recoil effect appears at both lower and higher energies, but it is more clearly seen at lower energy side because of the Coulomb barrier. For the EUGENE-GEMINI simulation (on the left) the helium spectrum is well reproduced with fission delay, whereas for the CHIMERA-GEMINI simulation the fit seems better without the fission delay. For protons the low energy part of the spectrum is better fit without fission delay for both simulations. On the higher energy side, the proton spectra show a high energy component even at the backward angles, compared to the model simulation, whereas the helium spectrum is well reproduced at this angle. This is also seen in the CHIMERA-GEMINI calculation. A similar high energy component is also seen in the deuteron and triton spectra (see Fig. 13) and these components are generally observed regardless of different neutron multiplicities.

IMF spectra are also compared to the simulations. In Fig. 6 the results of the CHIMERA-GEMINI calculation are shown for carbon energy spectra both with (dashed histogram) and without fission delay (solid histogram). The calculated spectra are normalized to the experimental data at $\theta = 39°$. As one can see, the experimental spectra at $\theta = 39°$ and 49° show a significant enhancement at the higher energy side. The discrepancy becomes larger when the EUGENE-GEMINI simulation is used.

In Fig. 11 the experimental charge distribution at $\theta = 39°$ is compared with the CHIMERA-GEMINI calculation both with and without fission delay. The calculated distributions are normalized to the experimental distribution at $Z = 2$. The calculated distribution with the fission delay gives

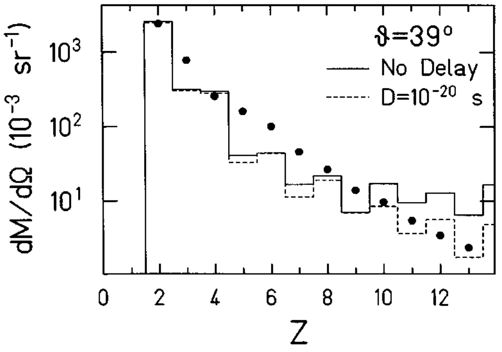

FIG. 11. Atomic charge distribution of IMF's emitted at $\theta=39°$. Experimental results are shown by solid symbols and histograms are the results from the CHIMERA-GEMINI simulation for no fission delay (solid) and a fission delay of 10×10^{-21} s (dashed). The calculated results are normalized to the experimental data at $Z=2$.

a slightly better fit at $Z\geq10$. For the IMF's with lower Z, both calculations underestimate the cross section by a factor of 2–5, except $Z=4$. The good agreement at $Z=4$ is artificial, because ^{8}Be is treated as a stable nucleus in the calculation. This yield difference originates from the high energy component, i.e., all light IMF's ($3\leq Z\leq 7$) show a significant high energy component in the energy spectra, which can not be reproduced by the simulations.

Calculated light particle and IMF multiplicities, associated with heavy fragments, are shown by histograms in Fig. 7 for the two fragment mass windows. The experimental light charged particle multiplicities were determined from the backward emitted particles, assuming a single source. Therefore the calculated light charged particle multiplicities are determined from particles emitted from the CN-like source in the case of the EUGENE simulation. For the CHIMERA simulation the light charged particle multiplicities are obtained by observing those particles emitted in the backward hemisphere in the moving source frame and then doubling their yield. IMF multiplicities are determined from IMF's emitted at the same angles as the experimental results. Generally the observed multiplicities associated with fission fragments are better predicted by the CHIMERA-GEMINI simulation, whereas those associated with the heavy remnants are better reproduced by the EUGENE-GEMINI simulation. In the above simulations a fission delay of 10×10^{-21} is applied for both calculations. In general, however, the different fission delays do not make a notable change in these multiplicities.

V. PROPERTIES OF HOT NUCLEI

A. Reconstruction of the primary composite system

The dynamical model CHIMERA predicts the formation of a hot composite nucleus in central collisions, whereas an equilibrated hot composite nucleus formation is assumed in the EUGENE calculation. The experimentally observed heavy remnants and fast fission fragments provide a strong indication of formation of such a nucleus, although there is a significant difference in the velocity distribution of the heavy remnants between the experimental and calculated results. It is very interesting, therefore, to reconstruct the mass and excitation energy from the experimental data and compare them to those obtained from the simulations.

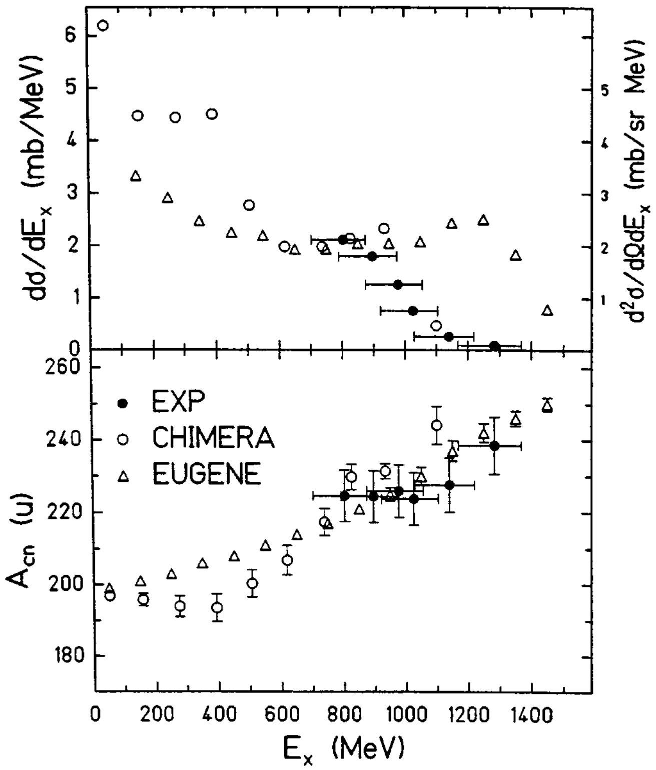

FIG. 12. (Top) Double differential cross section of the heavy remnant observed at $\theta=6°$. The results of the EUGENE calculation are plotted using open triangles and those of the CHIMERA calculation using open circles. The scale for the experiment is indicated on the right Y axis. Units are given in an absolute scale of mb/sr/MeV. The scale for the calculations is given on the left y axis in an absolute scale of mb/MeV. (Bottom) Primary composite nucleus mass vs excitation energy. The results reconstructed from the experimental observables are shown by the solid symbols. Symbols are the same as in the top part of the figure. The CHIMERA results for the mass and excitation energy are corrected for evaporated particles. See details in the text.

The calculated masses and excitation energies of the primary composite nuclei are shown in the lower part of Fig. 12 by open circles for the CHIMERA code and open triangles for the EUGENE calculation. For the CHIMERA calculation, mass and excitation energy of the primary heavy nuclei were calculated at $t=200$ fm/c and then corrected by estimating the mass and energy carried away by evaporative particles emitted before $t=200$ fm/c, which were evaluated by doubling the number of light particles emitted at the backward hemisphere in the moving source frame at $t=200$ fm/c. This procedure was also performed for events calculated at 300 fm/c and the extracted excitation energy agrees within 10 MeV for the highest remnant velocity window. For central collisions the calculated excitation energy for a given mass is slightly smaller in the CHIMERA calculation than that in the EUGENE calculation. This originates from the fact that the binding energy calculated in the CHIMERA code is slightly greater than that used in the empirical mass formula in the EUGENE code. In the upper part of Fig. 12 differential cross

TABLE I. Parameters used for the evaluation of the primary heavy remnants. V_R is the velocity of the heavy remnant in cm/ns. $\overline{M_i}$ and $\overline{E_i}$ (in MeV) are the average multiplicity and average energy of particle i.

V_R	$\overline{M_n}$ [a]	$\overline{E_n}$ [b]	$\overline{M_p}$	$\overline{E_p}$	$\overline{M_d}$	$\overline{E_d}$	$\overline{M_t}$	$\overline{E_t}$	$\overline{M_h}$	$\overline{E_h}$	$\overline{M_\alpha}$	$\overline{E_\alpha}$	$\overline{M_{Li}}$	$\overline{E_{Li}}$	$\overline{M_I}$	$\overline{E_I}$	Q value
0.625	33.6	6.0	4.4	15.7	1.4	21.4	0.8	22.6	0.2	30.3	3.9	23.2	0.4	50.6	0.6	71.4	303.0
0.875	35.4	6.4	5.1	15.5	1.6	21.9	1.0	22.4	0.2	30.8	4.5	23.8	0.4	52.0	0.7	69.7	326.1
1.125	35.7	6.8	5.7	16.6	1.7	22.9	1.2	24.2	0.3	35.6	4.8	25.7	0.4	45.4	0.7	76.1	343.7
1.375	36.1	7.2	5.4	17.8	2.0	24.3	1.3	26.1	0.3	34.6	5.1	26.5	0.5	43.8	0.7	77.1	348.1
1.625	37.4	7.6	6.8	17.3	2.4	28.8	1.5	26.4	0.4	33.0	5.7	29.4	0.4	51.1	0.7	64.5	363.5
1.875	38.7	8.2	7.9	18.8	2.9	27.8	1.6	29.6	0.4	36.3	6.3	32.7	0.6	48.0	0.7	70.2	372.8

[a] Efficiency corrected.

[b] Calculated.

sections are given for both simulations. The EUGENE simulation produces a large number of composite nuclei with $E_x \sim 1000-1400$ MeV, whereas in the CHIMERA code the cross section for such a composite nucleus vanishes quickly at 1000–1100 MeV.

From the experimental results the primary mass and the excitation energy of the composite system have been reconstructed in the following manner: First the events in which a heavy remnant ($A \geqslant 130$) is observed were selected. The mass and excitation energy are evaluated in the six different velocity windows of the heavy remnant. For each velocity window of the heavy remnants, the mass of the primary composite system was simply obtained by adding up all the evaluated charged particle multiplicities from the composite system, the efficiency corrected neutron multiplicity from the composite system and the observed mass of the heavy remnant. The efficiency corrected neutron multiplicity from the composite system was evaluated from the detected neutrons, using the calculated detection efficiency of the neutrons from the composite system. The excitation energy $E^*_{\rm cn}$ was calculated assuming;

$$E^*_{\rm cn}=\sum_i \left(\langle E^i_k\rangle\langle M_i\rangle\right)+Q+E_\gamma . \qquad (1)$$

Here $\langle E^i_k\rangle$ and $\langle M_i\rangle$ are, respectively, the average kinetic energy in the moving frame and the average multiplicity of the particle i. This determination included all atomic numbers up to $Z=10$. All these values are experimentally determined, except E_k for the neutrons, for each remnant velocity window. The average kinetic energy of neutrons was calculated using the simulation. Q is the reaction Q value and was calculated from the charges and masses of the observed particles. The mass to charge ratio of 2.4 was used to estimate the charge of the primary composite system. This is consistent with the results of the simulation. The remnant charge is that of the primary composite system minus the total charge removed by the observed charged particles. E_γ was assumed to be 20 MeV.

In order to correct for the contribution from the detection of preequilibrium neutrons in the detected neutron multiplicity, the number of the detected preequilibrium neutrons is evaluated for different velocity windows of the heavy remnants using the simulations. The extracted numbers in the EUGENE calculation are 1.2 for the lowest velocity window and 1.7 for the highest velocity window. For the CHIMERA simulation only the average number of the detected preequilibrium neutrons is evaluated, because of the low statistics. The average number of 2.5 is obtained by subtracting the detected neutron number (0.2) in the backward hemisphere from those (2.7) emitted in the forward hemisphere at $t=200$ fm/c.

The extracted masses and excitation energies of the primary composite system are plotted as the solid circles and compared to the calculated distributions from the simulations (open symbols) in Fig. 12. The experimentally extracted masses of the composite system remains more or less a constant for different excitation energies, except at the highest excitation energy, whereas in both simulations the masses show a slight increase with increasing excitation energy. For the most central collisions the experimentally evaluated mass and excitation energy of the primary composite system reach $A \sim 240$ and $E_x \sim 1280$ MeV, respectively. This excitation energy is between the maximum values derived from the two calculations, whereas the mass is consistent with those of the composite nucleus in the calculations. The values used for the evaluation are summarized in Table I for the different velocity windows of the heavy remnants and the extracted masses and excitation energies are given in Table II. The error bars in the experimental data points are estimated over all errors. The error for the mass determination reflects the experimental errors on the remnant mass and on the particle multiplicity determination. The error on the excitation energy primarily reflects the calculated average kinetic energy,

TABLE II. The extracted average masses and excitation energies of the primary heavy remnants. V_R (cm/ns) is the velocity of the heavy remnant. A_R (u), $A_{\rm cs}$ (u), and $E_{\rm cs}$ (MeV) are the average mass of the heavy remnant, the extracted primary mass, and the extracted excitation energy of the primary composite system, respectively.

V_R	A_R	$A_{\rm cs}$	$E^*_{\rm cs}$
0.625	155.4 ±2.8	224.6 ±7.4	803.6 +100.3/-70.3
0.875	148.1 ±2.6	224.4 ±7.2	895.9 +104.8/-79.8
1.125	146.3 ±2.6	225.9 ±7.3	978.0 +103.3/-78.3
1.375	142.1 ±2.5	223.8 ±7.2	1025.9 +103.8/-78.8
1.625	139.7 ±2.5	227.6 ±7.5	1139.8 +110.1/-80.1
1.875	143.1 ±3.0	238.5 ±8.4	1283.0 +114.3/-84.3

the number of preequilibrium neutrons in the detected neutron number and the Q-value estimation. The calculated neutron average kinetic energy depends on the level density parameter used. Therefore the value given in the Table I was obtained by averaging over the three calculations with $a=A/8.5$, $A/10$, and $A/13$ and the error assigned was obtained as a maximum deviation from the average values. The error in the average neutron energy was 0.35 MeV for the lowest velocity of the remnant and 0.56 MeV for the highest velocity. These give about 15–25 MeV energy uncertainty in the final results. The uncertainty from the Q value is estimated to be about 28–30 MeV for different assumptions of A/Z values of the primary composite system ($A/Z=2.3$–2.5). The number of detected preequilibrium neutrons in the different remnant velocity windows is taken from the EUGENE calculation. The difference from the CHIMERA calculation is taken into account in the error estimation.

In the upper part of Fig. 12 the experimental double differential cross section of these heavy remnants at $\theta=6°$ is plotted in an absolute scale given on the right. Since the calculated cross sections in the same figure are given in a single differential cross section form ($d\sigma/d\Omega dE_x$), one cannot directly compare to the experimental data. However as one can expect that the angular distribution of the heavy remnants is similar at forward angles for the different velocity windows, the shape of the double differential cross section is more or less similar to the angle-integrated cross section. The shape of the experimental cross section is similar to the result of CHIMERA calculation, but has a longer tail towards the higher energy side. One should note, however, that this experimental cross section was extracted only from the heavy remnants and the cross section on the higher energy side will be enhanced when the fission channel contribution is taken into account.

In the calculations the excitation energies shown in the lower part of Fig. 12 are treated as thermal energy and carried away by evaporative particles. For the experimentally extracted energies it should be noted that the proton energy spectrum shown in Fig. 5 has a harder energy component than that of the calculations, whereas the α spectrum is well reproduced by the simulations. The contribution of the hard component to the proton spectra, evaluated from the difference between the experimental and calculated spectra, is about 10–15% of the total yield at backward angles. The information for the neutron energy spectra is not available in this experiment.

While one might also estimate the excitation energy deposition by comparing selected evaporated particle neutron multiplicities with results of the model calculations, given the discrepancies between calculation and experiment observed in Fig. 7, application of such a technique does not appear justified here. It is interesting to note that, in studies of the binary collisions of ^{208}Pb + ^{197}Au at 29A MeV [41] excitation energies for each of the partners in the most dissipative binary collisions have been found to be $\sim 5A$ MeV. In that work, the measured evaporated neutron multiplicities, obtained with discrete detectors, have been reported as $\sim$ 60, i.e., 30 per fragment with $A\sim 200$. These results appear to be quite consistent with those derived for the fusionlike central collisions seen in our work.

B. Temperature determinations

1. Experimental results

Determining the temperatures of highly excited nuclei such as those studied here has proved to be difficult. Effects of reaction dynamics and secondary decays, coupled with inherent mechanism questions, can lead to significant uncertainties in ‘‘temperature’’ measurements. The measurements of spectral slopes, traditionally used at lower energies to extract temperatures [42,43], become less useful at very high energies due to dynamical effects. Alternative measurements employing ratios of excited states [44–46] or double isotope ratios [18–21,26] offer some potential advantages in that they may be less susceptible to some of the dynamic effects which render the slope measurements suspect. At the same time, questions of sequential decay effects, both in the production of primary fragments and in the subsequent deexcitation of the species employed in these ratio measurements [20,21,47], together with the ever present questions of production mechanism mean that, even in the ratio measurements, care must be taken in interpreting the observed results in terms of temperatures.

One recent study of the isotope ratio method was carried out by Tsang *et al.* [20] who have derived isotope temperatures for the reactions of 35A MeV ^{40}Ar with ^{197}Au, and have indicated that modifications of the He-Li ratios resulting from secondary decay processes require detailed information on product mass distributions to make these ratios suitable as thermometers. While our system, 35A MeV ^{63}Cu + ^{197}Au is similar to that studied by Tsang *et al.*, somewhat higher excitation energies are realized and can be selected using the velocity and/or particle multiplicity data. Thus it is interesting to see what can be learned from an exploration of the double isotope ratio temperatures in our system.

To pursue these measurements we have used data from the backward angle detectors in our second experiment to determine the spectra of H, He, Li, and Be isotopes, either in coincidence with the heavy fragments or, using the self-triggering mode of the neutron ball, as a function of neutron multiplicity. Using the backward angle detectors for this purpose resulted in significant energy thresholds for identifying the Li and Be isotopes but reduced the possible contributions from projectile like sources. The observed energy spectra are shown in Fig. 13. Solid points are experimental data and histograms are from the EUGENE-GEMINI simulations with and without fission delay. Except for the He isotopes the isotope pairs used show very similar energy spectra. The difference observed in the ^{3}He and ^{4}He spectra have been noted previously in other studies [20,48]. Tsang *et al.* attribute the differences to an enhancement of ^{4}He at the lower kinetic energies reflecting the more favored evaporation of ^{4}He at the lower energies sampled during the deexcitation cascade. This explanation appears quite reasonable.

In Fig. 14 we present, as a function of observed neutron multiplicity, isotope ratios determined from our measurements. Based on the results in the Sec. V A, we estimate that these ratios span an excitation energy range from 3.6 to 5.3A MeV. Spectra used in these experiments were taken at $\theta=110°$. Using the technique of Albergo *et al.*, but ignoring all questions of the effect of population of decaying excited

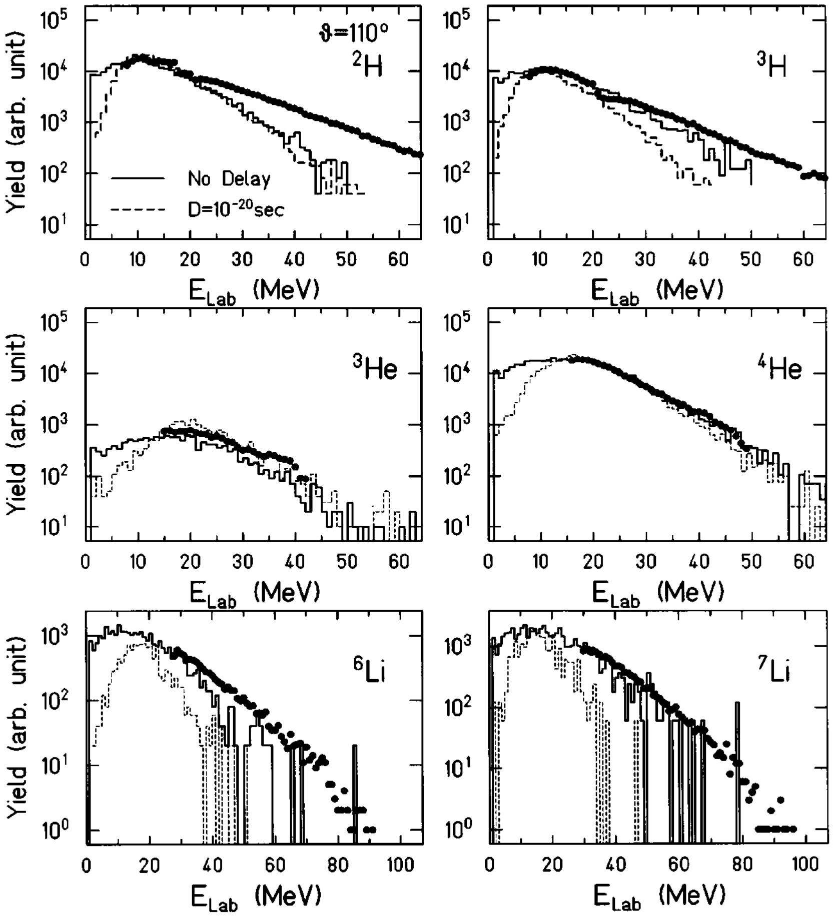

FIG. 13. Typical isotope energy spectra at $\theta = 110°$, used for the temperature evaluation. The solid and dashed histograms are results of the EUGENE-GEMINI simulation without delay and with a fission delay of 10×10^{-21} s. The calculated results are normalized to the experimental data individually.

states or secondary decay on the ratios, double isotope ratio temperatures can be extracted. The formula used is taken from [26],

$$T = \frac{B}{\ln(aR)} \tag{2}$$

where

$$B = BE(A_i,Z_i) - BE(A_i+1,Z_i) + BE(A_j,Z_j) - BE(A_j+1,Z_j), \tag{3}$$

$$R = \frac{Y(A_i,Z_i)/Y(A_i+1,Z_i)}{Y(A_j,Z_j)/Y(A_j+1,Z_j)}, \tag{4}$$

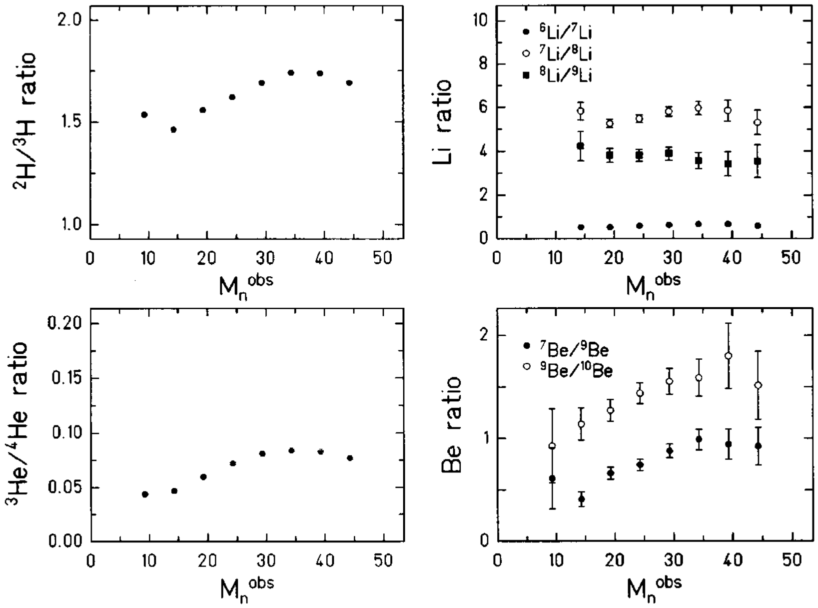

FIG. 14. Isotope yield ratios for light isotope products as a function of the associated neutron multiplicity. Only the backward angle telescopes have been used to determine these ratios. The results for different isotope pairs are presented as a function of the detected neutron number corrected for the background. Error bars are shown when statistical errors exceed the size of the symbol.

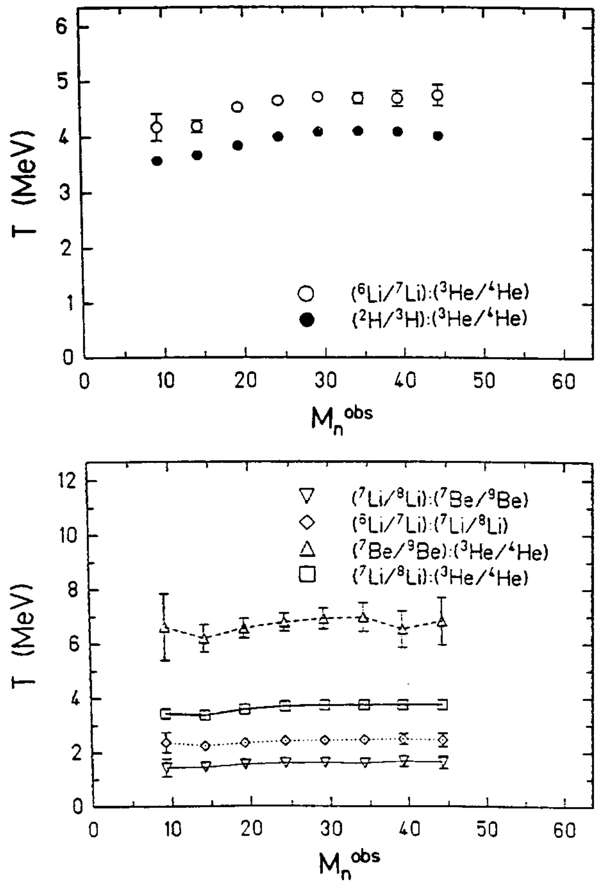

FIG. 15. Apparent temperatures calculated from the observed double isotope ratios using Eqs. (2)–(5). No corrections have been made for sequential decay effects. See text and Fig. 16. Solid and open circles in the top figure are derived from the ratios of (^{2}H/^{3}H)/(^{3}He/^{4}He) and (^{6}Li/^{7}Li)/(^{3}He/^{4}He), respectively. Shown in the bottom are results for (^{7}Li/^{8}Li)/(^{7}Be/^{9}Be) (downward triangle), (^{6}Li/^{7}Li)/(^{7}Li/^{8}Li) (diamond), (^{7}Li/^{8}Li)/(^{3}He/^{4}He) (square), and (^{7}Be/^{9}Be)/(^{3}He/^{4}He) (upward triangle).

$$a=\frac{[2S(A_j,Z_j)+1]/[2S(A_j+1,Z_j)+1]}{[2S(A_i,Z_i)+1]/[2S(A_i+1,Z_i)+1]}\left(\frac{A_j/(A_j+1)}{A_i/(A_i+1)}\right)^{3/2}. \tag{5}$$

Here $Y(A_i,Z_i)$, $BE(A_i,Z_i)$, $S(A_i,Z_i)$ are the yield, binding energy, and spin of the ground state of a specific isotope with mass A_i, and Z_i. The derived temperatures from several isotope pairs are presented in Fig. 15 as a function of associated neutron multiplicity. These temperatures show some variation with neutron multiplicity, but tend toward essentially constant values at the largest multiplicities. Assuming a similar mechanism of production for the observed isotopes, the wide variation of the derived temperatures confirms that a more detailed treatment is required to extract meaningful information.

In the spirit of earlier isotope ratio and state ratio measurements it is certainly of interest to see whether a self-consistent treatment of the full set of observed yields and yield ratios can lead to the extraction of a single primary temperature of the deexciting system [20,49]. A model to attempt this has been constructed by Kolomiets *et al.* [49]. The statistical model with chemical equilibrium condition [26] was used to find population of excited states of fragments. The population of the excited states which decay on the way to the detector by γ or particle emission into the ground state of the fragments were taken into account to calculate experimentally measured yields. The ratios of yields at $M_n^{\rm obs}=28$ were then used to extract the temperature. The results obtained are shown in Fig. 16. We used experimentally measured excited states from [50,51]. The values of binding energies were taken from [52]. Following assumptions made in [49], the particle-decay feeding of ^{3}He, ^{4}He as well as ^{2}H and ^{3}H ground populations was ignored. We took only the double ratios for those pairs which have a sufficiently large value of B of Eq. (3), in order to avoid a strong sensitivity of the extracted temperature on the experimental error [21]. On the left side of Fig. 16 temperatures without the feeding correction are plotted. One can see large fluctuations. In the middle are presented the results when only γ-decay feeding is taken into account. A significant decrease of the fluctuations is observed. On the right side of Fig. 16 temperatures derived correcting for combined feedings of both γ and particle decay are plotted. This combined feeding is an estimation at this stage because of the lack of comprehensive experimental information on the excited states of nuclei. Most of the derived temperatures are in the range of 4–5 MeV. In particular, our derived $T_{\rm HeLi}$ temperatures are quite similar to these observed for heavy nuclei ($A\sim190$) by the ALADIN [18] and EOS Collaborations [19], as well as to those obtained by Tsang *et al.* [20], although for such nuclei our data extend to somewhat higher excitation energy.

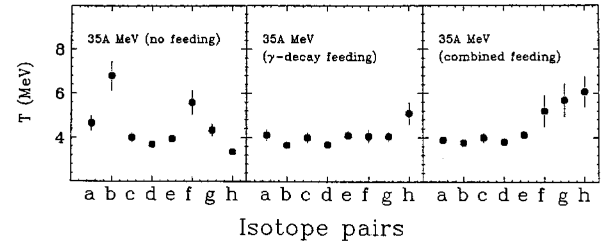

FIG. 16. Temperatures derived from double isotope ratios when $M_n=28$. (Left) Temperatures derived using Eqs. (2)–(5) which ignores excited state population and decay. (Middle) Temperatures derived with population and γ decay of known excited states included. (Right) Temperatures derived including population of known states together with γ and particle decay. Results in the latter two panels contain corrections calculated using the model of Kolomietz *et al.* [48]. Letters on the x axis indicate the ratios used a; (^{6}Li/^{7}Li)/(^{3}He/^{4}He), b;(^{9}Be/^{10}Be)/(^{3}He/^{4}He), c;(^{2}H/^{3}H)/(^{3}He/^{4}He), d;(^{7}Li/^{8}Li)/(^{3}He/^{4}He), e;(^{8}Li/^{9}Li)/(^{3}He/^{4}He), f;(^{6}Li/^{8}Li)/(^{7}Be/^{9}Be), g;(^{7}Li/^{9}Li)/(^{7}Be/^{9}Be), h;(^{6}Li/^{9}Li)/(^{7}Be/^{10}Be).

2. Model comparisons

As noted, the interpretation of these results still demands assumptions about the emission mechanism. To probe this question one can consider the two extreme cases of purely simultaneous emission or purely sequential emission of the isotopes observed. The former case has recently been treated by Majka *et al.* using a quantum statistical model [53]. The results of that calculation show that at temperatures greater than 4–5 MeV large numbers of fragments can result at freezeout. In the high temperature region the calculated isotope ratios reflect the freezeout temperature. However, the apparent temperatures determined from the isotope ratios are lower than the freezeout temperature. In such a scenario isotope ratio apparent temperatures near 4 MeV observed in our work would indicate a freezeout temperature of ~ 5 MeV. In this range the quantum statistical model suggests that a large excited cluster is very probable.

In Sec. V A we have already noted that the 29*A* MeV ^{208}Pb + ^{197}Au collision which has been extensively studied using the GANIL accelerator [41] leads to the production of $A\sim200$ nuclei at excitation energies of $\sim5A$ MeV, similar to those in the present work. Measurements of α particle spectra for that system have led to the conclusion that apparent temperatures of 4.5–6.9 MeV are seen [54]. Based on those results the argument has been made that the initial temperatures in this mass range are higher than those reported in the ALADIN and EOS work and support a sequential decay mechanism of IMF production.

In a sequential decay model the isotope ratios would also be expected to vary with the particle kinetic energy in the source frame, reflecting the emission of higher energy particles early in the cascade. To search for such an effect in our data, we have divided the observed He and Li spectra in the source frame into three bins of kinetic energy above the barrier and derived the isotope ratio temperatures corresponding to the three different bins. The results, at higher excitation show an increase in T of ~1 MeV with increasing fragment kinetic energy. This is similar to the increase calculated using EUGENE-GEMINI and suggests that sequential decay may, in fact, be important in this system.

We have also used calculations with the combined EUGENE-GEMINI code to explore the relationship between the initial input temperature and the apparent temperature derived from the yield calculations in a sequential model. Results of these calculations are summarized in Fig. 17. Here we note that temperatures, derived from the double ratios between yields of the first chance emission hydrogen and helium isotopes, are quite close to the calculated initial temperatures. On the other hand, those derived from first chance helium and lithium isotope emission yields are well below the initial temperature. If the entire deexcitation cascade is sampled, then both apparent temperatures are similar and in the range 4–5 MeV, but much lower than the initial temperatures of 5.5–7.5 MeV, as expected in such a sequential model. This model calculation includes secondary emission from the IMF's, but only in a purely statistical approach without inclusion of detailed information on low lying states in the IMF. Clearly an unambiguous determination of the mechanism of IMF production is required before an appropriate interpretation of the temperatures derived from isotope ratios can be made.

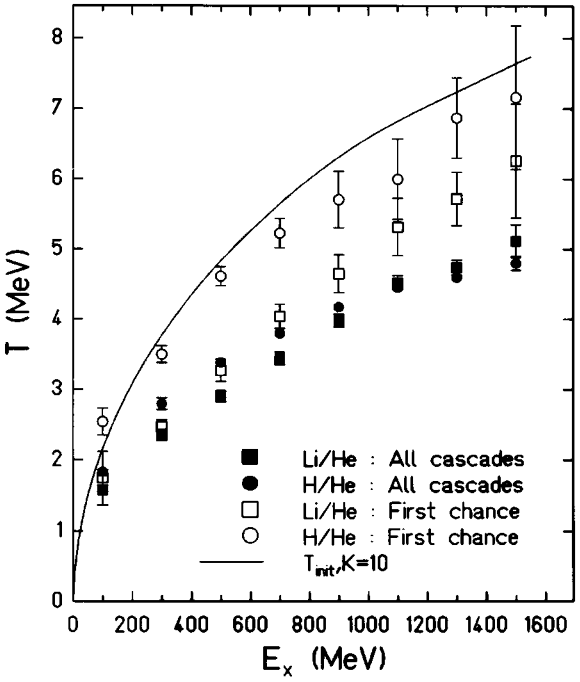

FIG. 17. Double isotope ratio temperatures in a sequential model. Using the EUGENE-GEMINI code the temperatures from the isotope ratios of (^{6}Li/^{7}Li)/(^{3}He/^{4}He) and (^{2}H/^{3}H)/(^{3}He/^{4}He) have been determined from the calculated ratios for first chance emission (open symbols) and for emission over the entire deexcitation cascade (solid symbols). The solid line indicates T$_{\rm init}$ for the assumed inverse level density parameter of $K=10$. See details in the text.

VI. SUMMARY AND CONCLUSIONS

We have presented results of a study of excitation energy deposition and evacuation in the reaction of 35*A* MeV ^{63}Cu on ^{197}Au. Heavy remnants with mass ~130–170 were observed at laboratory angle of $\theta=6°$ with velocities between 0.5 to near 2.0 cm/ns. These fragments are associated with high neutron and charged particle multiplicities. These multiplicities increase as the remnant velocity increases. A similar behavior is also observed for fission-like fragments detected at the same angle. These results suggest that a hot composite nucleus is formed in an incomplete fusion or massive transfer process. The masses and excitation energies of the primary composite system have been reconstructed for the events in which heavy remnants are observed. The reconstructed masses of the primary nucleus are ~225–240 and the excitation energies are 3.6–5.3*A* MeV. The highest excitation energy extracted is ~1280 MeV for the primary mass of ~240.

The experimental results are compared with those of model simulations, which are based on the massive transfer code EUGENE-GEMINI and the quantum dynamical model code CHIMERA-GEMINI. The maximum excitation energy of the primary composite system derived from the experimental data is in between the predicted excitation energies of the primary composite nucleus of the two models, whereas the reconstructed mass is consistent with those in the model simulations. The observed trend of the particle multiplicities as a function of the velocity of the associated fission fragments and heavy remnants is well reproduced by the two model simulations. On the other hand the observed mass of the heavy remnants can not be reproduced by both models without incorporation of the fission delay. Even with incorporation of the fission delay in both simulations, however, the experimental trend of the heavy remnant velocity is not reproduced. This may indicate that the entrance channel dynamics treated in both models is insufficient and some important mechanisms, which leads to the production such heavy remnants, are missing in these treatment. Although the EUGENE program is designed for a event generator and uses a simple treatment of the entrance channel dynamics [10], it reproduces the experimental results almost as well as the QMD does. This may indicate that, in this energy region, the reaction dynamics is governed by the preequilibrium emission and no exotic process such as a simultaneous multifragmentation is yet taking place.

Pollaco *et al.* reported a similar heavy remnant observation in the study of ^{40}Ar$+^{232}$Th at 27–77A MeV [13,15]. In their analysis they found that the yield of the heavy remnants observed at forward angles is significantly enhanced when an additional IMF coincidence is required and they are associated with two IMF's on average. In our simulations shown above, the calculated IMF multiplicity from the compound system is of the order of one and the higher energy component of the IMF energy spectrum is missing. This may suggest that an IMF is emitted at an early stage even for central or midcentral collisions.

Recently Ono and Horiuchi [55] applied antisymmetrized quantum molecular dynamics (AMD) to the data for ^{40}Ca$+^{40}$Ca at 35A MeV [56] and made a significant improvement of the fits to the experimental results, compared to a QMD calculation. It is very interesting that the incorporation of the antisymmetrization in the quantum molecular dynamics makes a drastic change in the reaction dynamics, especially in the emission of the IMF's. Many IMFs are emitted at very early stages of the reaction. This may affect significantly the formation of the hot compound nucleus. Unfortunately we cannot presently apply the AMD to our system because of the huge computing time required. For the present AMD framework, the computing time increases by A^4, where A is the total mass of the system.

Double isotope ratio measurements have been used in an attempt to derive source temperatures using the technique proposed by Albergo *et al.* [26]. When emission temperatures are derived from the observed isotope yield ratios by taking into account the population and decay of excited states in a self-consistent way, apparent temperatures of 4–5 MeV are derived for the most excited nuclei, $E^* \sim 5.3A$ MeV. Those are similar to temperatures derived for similar mass nuclei in other recent experiments [18–21]. However the interpretation of these results is subject to model assumptions and there is some evidence that production of IMF in a sequential decay cascade is important in this system.

In closing we note that in some recent work, temperature determinations based on the measurements of double isotope ratios have been used to probe nuclei with initial excitation energies as high as 15A MeV [18,19]. Interesting trends in the ''caloric curves'' extracted from such measurements have been noted. It has been proposed that the transition to a vapor stage is signaled by this temperature evolution [18]. The data presented have usually spanned a significant range of isotope masses and it was suggested, by us, that the mass dependence of the temperatures may have much to do with the observed trends [57]. We also suggested that, for a single mass near $A\sim125$, a much smaller variation of T with excitation is indicated by the available data. This appears to be confirmed by a comparison of the ALADIN results [18] with recently published EOS results [19]. The latter show significantly lower isotope temperatures at 15A MeV excitation energy. This may result from the fact that the masses of the deexciting systems sampled at that excitation are much different in the EOS data than in the ALADIN data. Taken together the two results show that, for $A\sim125$, there is little change in the isotope ratios and thus in the derived limiting temperature from 11 to 15A MeV. Given the uncertainties in interpretation of those ratios the results are reasonably consistent with the $A\sim125$ data at lower excitation energies and suggest relatively little change in the limiting temperature from 3 to 15A MeV. On the other hand, as indicated in Sec. V B, further explorations of the applicability and sensitivity of the double isotope ratio method are needed before this result is considered validated.

ACKNOWLEDGMENTS

We thank D. Durand for providing us the EUGENE code and R. J. Charity for the GEMINI code. We especially acknowledge the operating staff in the Cyclotron Institute for their excellent job during our beam time. This research was supported by U.S. Department of Energy under Grant No. DE-FE05-86ER40256, by the Robert A. Welch Foundation, and by the Polish Scientific Research Committee under Grant No. 2 2392 91 02.

---

[1] A good review in this field will be found in *Proceedings of the Symposium on Nuclear Dynamic and Nuclear Disassembly*, edited by J. B. Natowitz (World Scientific, Singapore, 1989).

[2] D. Guerreau, in *Nuclear Matter and Heavy Ion Collisions*, edited by M. Soyeur, H. Flocard, B. Tamain, and M. Porneuf (Plenum Press, New York, 1989), p. 187, and references therein.

[3] M. T. Magda and J. M. Alexander, in *Topics in Atomic and Nuclear Collisions*, edited by B. Remaud (Plenum Press, New York, 1994), p. 97.

[4] D. H. E. Gross, Rep. Prog. Phys. **53**, 605 (1990), and references therein.

[5] B. Tamain, University of Caen Report LPCC 90-12, (1990), and references therein.

[6] C. Gregoire and B. Tamain, Ann. Phys. (Paris) **11**, 323 (1986), and references therein.

[7] Proceedings of the Symposium on the Many Faces of Heavy-Ion Fusion Reactions, edited by W. Henning, D. Kovar, S. Landowne, and S. Pieper [Argonne National Laboratory Report No. ANL-PHY-86-1 (1986)].

[8] B. G. Harvey and M. G. Murray, Phys. Lett. **130B**, 373 (1983); B. G. Harvey, Nucl. Phys. **A444**, 498 (1985).

[9] H. Fuchs and K. Mohring, Rep. Prog. Phys. **57**, 231 (1994), and references therein.

[10] D. Durand, Nucl. Phys. **A541**, 266 (1992).

[11] D. Utley, R. Wada, K. Hagel, J. Li, B. Xiao, M. Gui, Y. Lou, R. Tezkratt, J. B. Natowitz, and M. Gonin, Phys. Rev. C **49**, R1737 (1994).

[12] W. Skulski, B. Djerroud, D. K. Agnihotri, S. P. Baldwin, W. U. Schröeder, J. Toke, X. Z. Zhao, L. G. Sobtka, R. Charity, J. Dempsy, D. G. Sarantites, B. Lott, W. Loveland, and K. Aleklett, University of Rochester Report UR-NSRL-408, 1996.

[13] E. C. Pollaco, E. Berthoumieux, E. De Filippo, C. Volant, R. Barth, B. Berthier, Y. Cassagnou, Sl. Cavallaro, J. L. Charvet, A. Cunsolo, M. Colonna, R. Dayras, D. Durand, A. Foti, S. Harar, G. Lanza/'no, R. Legrain, V. Lips, C. Mazur, E. Norbec, H. Oeschler, A. Pagano, and S. Urso, Nucl. Phys. **A583**, 441 (1995).

[14] E. Schwinn, U. Janke, J. L. Charvet, B. Cramer, H. Doubre, J. Fréhaut, J. Galin, B. Gatty, D. Guerreau, G. Ingold, D. Jacquet, D. X. Jiang, B. Lott, M. Morjean, C. Magnago, Y. Patin, J. Pouthas, E. Piasecki, and A. Sokolov, Nucl. Phys. **A568**, 169 (1994).

[15] E. Berthounieux, E. C. Pollacco, C. Volant, E. De Fillipo, R. Barth, B. Berthier, Y. Cassagnou, Sl. Cavallaro, J. L. Charvet, M. Colonna, A. Cunsolo, R. Dayras, D. Durand, A. Foti, S. Harar, G. Lanza/'no, R. Legrain, V. Lips, C. Mazur, E. Norbec, H. Oeschler, A. Pagano, and S. Urso (unpublished).

[16] R. J. Charity, M. A. McMahan, G. J. Wozniak, R. J. McDonald, L. G. Moretto, D. G. Sarantites, L. G. Sobotka, G. Guarino, A. Pantaleo, L. Fiore, A. Gobbi, and K. D. Hildenbrand, Nucl. Phys. **A483**, 371 (1988).

[17] J. Lukasik and Z. Majka, Acta Phys. Pol. B **24**, 1959 (1993).

[18] J. Pochodzalla, T. Möhlenkamp, T. Rubehn, A. Schüttauf, A. Wörner, E. Zude, M. Begemann-Blaich, Th. Blaich, C. Gross, H. Emling, A. Ferrero, G. Imm/'e, I. Iori, G. J. Kunde, W. D. Kunze, V. Lindenstruth, U. Lynen, A. Moroni, W. F. J. Müller, B. Ocker, G. Raciti, H. Sann, C. Schwarz, W. Seidel, V. Serfling, J. Stroth, A. Trzcinski, W. Trautmann, A. Tucholski, G. Verde, and B. Zwieglinski, Phys. Rev. Lett. **75**, 1040 (1995).

[19] J. A. Hauger *et al.*, Phys. Rev. Lett. **77**, 235 (1996).

[20] M. B. Tsang, F. Zhu, W. G. Lynch, A. Aranda, D. R. Bowmann, R. T. de Souza, C. K. Gelbke, Y. D. Kim, L. Phair, S. Pratt, C. Williams, H. M. Xu and W. A. Friedman, Phys. Rev. C **53**, R1057 (1996).

[21] M. B. Tsang, W. G. Lynch, and W. A. Friedman, NSCL Report MSUCL-1035, 1996.

[22] R. P. Schmitt, L. Cooke, G. Derrig, D. Fabris, B. Hurst, J. B. Natowitz, G. Nebbia, D. O'Kelly, B. K. Srivastava, W. Turmel, D. Utley, H. Utsunomiya, R. Wada, Nucl. Instrum. Methods Phys. Res. A **354**, 487 (1995).

[23] J. Poitou and C. Signarbieux, Nucl. Instrum. Methods **114**, 113 (1974).

[24] J. Lukasik, M. Micek, Z. Sosin, A. Wieloch, and K. Grotowski, Nucl. Instrum. Methods Phys. Res. A **274**, 265 (1980).

[25] T. C. White, J. A. Wigner, H. Johnston, S. J. Yennello, TAMU Cyclotron Progress Report, 1993, p. V-146.

[26] K. Albergo, S. Costa, E. Constanzo, and A. Rubbino, Nuovo Cimento A **89**, 1 (1985).

[27] R. P. Schmitt, *Proceedings of the International Conference on New Nuclear Physics with Advanced Technique* (World Scientific, Singapore, 1992), p. 182.

[28] A. Sokolov, D. Guerreau, J. L. Charvet, B. Cramer, H. Doubre, J. Fréhaut, J. Galin, B. Gatty, G. Ingold, D. Jacquet, U. Jahnke, D. X. Jiang, B. Lott, C. Magnaro, M. Morjean, Y. Patin, E. Piasecki, J. Pouthas, and E. Schwinn, Nucl. Phys. **A562**, 273 (1993).

[29] W. Skulski, B. Djerroud, D. K. Agnihotri, S. P. Baldwin, W. U. Schröeder, J. Toke, X. Z. Zhao, L. G. Sobtka, R. Charity, J. Dempsy, D. G. Sarantites, B. Lott, W. Loveland, and K. Aleklett, Phys. Rev. C **53**, R2594 (1996).

[30] E. Vient, Ph.D. thesis, University of Caen, 1992; E. Vient, A. Badala, R. Barbera, G. Bizard, R. Bougault, R. Brou, D. Cussol, J. Colin, D. Durand, A. Drouet, J. L. Laville, C. Le Brun, J. F. LeColley, M. Louvel, J. P. Patry, J. Péter, R. Régimbart, J. C. Steckmeyer, B. Tamain, A. Peghaire, P. Eudes, F. Guilbault, C. Lebrun, E. Rosato, and A. Oubahadou, Nucl. Phys. **A571**, 588 (1994).

[31] J. Aichelin and H. Stöcker, Phys. Lett. B **176**, 14 (1986); J. Aichelin, G. Peilert, A. Bohnet, A. Rosenhauer, H. Stöcker, and W. Greiner, Phys. Rev. C **37**, 2451 (1988); G. Peilert, H. Stöcker, W. Greiner, A. Rosenhauer, A. Bohnet, and J. Aichelin, *ibid.* **39**, 1402 (1989); J. Aichelin, Phys. Rep. **202**, 233 (1991).

[32] D. Boal and J. K. Gloski, Phys. Rev. C **38**, 2621 (1988).

[33] J. Cibor, J. Lukasik, and Z. Majka, Z. Phys. A **248**, 233 (1994).

[34] F. Haddad, J. B. Natowitz, B. Jouault, V de la Mota, G. Royer, and F. Sebille, Phys. Rev. C **53**, 1437 (1996).

[35] H. Hauser and H Feshbach, Phys. Rev. **87**, 366 (1952).

[36] L. G. Moretto, Nucl. Phys. **A247**, 211 (1975).

[37] J. Cibor, Z. Majka, T. Kozik, P. Staszel, Z. Sosin, K. Hagel, J. Li, Y. Lou, R. Tezkratt, D. Utley, R. Wada, B. Xiao, and J. B. Natowitz, Phys. Rev. C **55,** 264 (1997).

[38] D. Hilscher and H. Rossner, Ann. Phys. (Paris) **17**, 471 (1992).

[39] D. Hinde, D. Hilsher, H. Rossner, B. Gebauer, M. Lehmann, and M. Wilpert, Phys. Rev. C **45**, 1229 (1992).

[40] M. Gui, K. Hagel, R. Wada, Y. Lou, D. Utley, B. Xiao, J. Li, J. B. Natowitz, G. Enders, W. Kühn, V. Metag, R. Novotny, O. Schwalb, R. J. Charity, R. Freifelder, A. Gobbi, W. Henning, K. D. Hildenbrand, R. Mayer, R. S. Simon, J. P. Wessels, G. Casini, A. Olmi, and A. A. Stefanini, Phys. Rev. C **48**, 1791 (1993).

[41] B. M. Quednau, S. P. Baldwin, B. Lott, W. U. Schröeder, B. M. Szabo, J. Tõke, D. Hilscher, U. Jahnke, H. Rossner, S. Bresson, J. Galin, D. Guerreau, M. Morjean, and D. Jacquet, Phys. Lett. B **309**, 10 (1993).

[42] R. Wada, D. Fabris, K. Hagel, G. Nebbia, Y. Lou, M. Gonin, J. B. Natowitz, R. Billerey, B. Cheynis, A. Demeyer, D. Drain, D. Guinet, C. Pastor, L. Vagneron, K. Zaid, J. Alarja, A. Giorni, D. Heuer, C. Morand, B. Viano, C. Mazur, C. Ngo, S. Leray, R. Lucas, M. Ribrag, and E. Tomasi, Phys. Rev. C **39**, 497 (1989).

[43] M. Gonin, L. Cooke, K. Hagel, Y. Lou, J. B. Natowitz, R. P. Schmitt, B. Srivastava, W. Turmel, H. Utsunomiya, R. Wada, G. Nardelli, G. Nebbia, G. Viesti, R. Zanon, G. Prete, P. Gonthier, and B. Wilkins, Phys. Lett. B **217**, 406 (1989).

[44] T. K. Nayak, T. Murakami, W. G. Lynch, K. Swartz, D. J. Fields, C. K. Gelbke, Y. D. Kim, J. Pochodzalla, M. B. Tsang, H. M. Xu, F. Zhu, and K. Kwiatkowski, Phys. Rev. C **52**, 1029 (1989).

[45] G. J. Kunde, J. Pochodzalla, J. Aichelin, E. Berdermann, B. Berthier, C. Cerruti, C. K. Gelbke, J. Hubele, P. Kzeutz, S. Leray, R. Lucas, U. Lynen, U. Milkau, W. F. Müller, C. Ngô, C. H. Pinkenberg, G. Raciti, H. Sann, and W. Trautmann, Phys. Lett. B **272**, 202 (1991).

[46] D. Morrissey, W. Benenson, and W. A. Friedman, Annu. Rev. Nucl. Sci. **44**, 65 (1994).

[47] J. B. Natowitz, J. C. Hagel, R. Wada, B. Xiao, J. Li, Y. Lou, and D. Utley, Phys. Rev. C **48**, 2074 (1993).

[48] K. G. R. Doss *et al.*, Mod. Phys. Lett. A **3**, 849 (1988).

[49] A. Kolomiets, E. Ramakrishnan, H. Johnston, F. Gimeno-Nogues, B. Hurst, D. O'Kelly, D. J. Rowland, S. Shlomo, T. White, J. Wigner, and S. J. Yennello, Phys. Rev. C **54**, R472 (1996).

[50] F. Ajzenberg-Selove, Nucl. Phys. **A490**, 1 (1988); **A506**, 1 (1990;); **A523**, 1 (1991); **A475**, 1 (1987).

[51] D. R. Tilly, H. B. Weller, and C. M. Cheves, Nucl. Phys. **A564**, 1 (1993).

[52] G. Audi and A. H. Wapsta, Nucl. Phys. **A565**, 1 (1993).

[53] Z. Majka, P. Staszel, J. B. Natowitz, J. Cibor, K. Hagel, J. Li, N. Mdeiwayeh, R. Wada, and Y. Zhao, Phys. Rev. C (to be published).

[54] M. Morjean, C. Lebrun, D. Ardouin, A. Chbihi, H. Dabrowski, B. Erazmus, P. Eudes, J. Galin, D. Guerreau, F. Guilbault, C. Ghisalberti, D. Jacquet, P. Lautridou, R. Lednicky, A. Péghaire, Y. Périrer, J. Pluta, L. Sezac, and R. H. Siemssen, Nucl. Phys. **A591**, 371 (1995).

[55] A. Ono and H. Horiuchi, Phys. Rev. C **53**, 2958 (1996).

[56] K. Hagel, M. Gonin, R. Wada, J. B. Natowitz, F. Haddad, Y. Lou, M. Gui, D. Utley, B. Xiao, J. Li, G. Nebbia, D. Fabris, G. Prete, J. Ruiz, D. Drain, B. Chambon, B. Cheynis, D. Guinet, X. C. Hu, A. Demeyer, C. Pastor, A. Giorni, A. Lleres, P. Stassi, J. B. Viano, and P. Gonthier, Phys. Rev. C **50**, 2017 (1994).

[57] J. B. Natowitz, K. Hagel, R. Wada, Z. Majka, P. Gonthier, J. Li, N. Mdeiwayeh, B. Xiao, and Y. Zhao, Phys. Rev. C **52**, R2322 (1995).